Novel Magnetically Levitated 2-Level Motor

***Abstract*– Several processes in chemical, pharmaceutical, biotechnology and semiconductor industry require contactless levitation and rotation through a hermetically closed chamber wall. This paper presents a novel concept that combines crucial advantages such as high acceleration capability, large air gap and a compact motor setup. The basic idea is to separate a homopolar bearing unit axially from a multipolar drive unit on two different height levels. Hence, the proposed concept is denominated as "Magnetically Levitated 2-Level Motor". In this paper, the bearing and drive functionalities are explained in detail and design guidelines are given based on analytic equations and electromagnetic 3D simulations. Furthermore, the influence of non-idealities such as saturation and coupling effects are evaluated and included in the design. Finally, extensive measurements on an experimental prototype exemplify the design considerations and prove the excellent performance of the new concept.**

I. Introduction

In the past decades there have been a lot of research activities in the field of magnetically levitated motors [1] - [6]. The implementation of the magnetic bearing technology includes key features such as contactless operation, almost unlimited life contrary to [7], build in fault diagnostics [8], wearless and lubrication-free operation and therefore a high level of purity [9] and the possibility of active vibration damping [10],[11]. In the pharmaceutical, chemical, biochemical and semiconductor industry several processes (e.g. coating, cleaning and polishing) require the application of chemical substances on rotating objects under clean room conditions [12]. Here, magnetically levitated motors are of high interest for these applications. The advantage of the magnetically levitated motors in these sensitive processes is their ability to spin a rotor in an encapsulated chamber, where the demand for high purity is satisfied and locally limited clean room space can be provided while avoiding failure susceptible seals.

Fig. 1 demonstrates schematically such a process, showing a levitated rotor carrying a process object. The process is enclosed by a chamber and the rotor is levitated and accelerated through the process chamber walls by the aid of electromagnetic bearings and drives, respectively. Basically, there are several requirements for these applications:

- A big air gap is required in order to ensure a minimum thickness and therefore mechanical robustness of the process chamber that is placed within the air gap.
- A compact motor setup is desirable due to the constantly increasing costs of clean room space.
- A high acceleration capability is needed in order to minimize the times between the process rotation speeds. This is directly influencing the efficiency and therefore the operating costs of the equipment.
- A maximum rotation speed required by the process has to be reached.
- A high temperature resistance is needed, including thermal expansion issues.
- A highly chemical resistant hardware setup avoids that the various strongly reactive chemicals degenerate the motor components.
- A stable, vibration-free levitation and rotation has to be ensured within the whole operating range, i.e. potential axial, radial and tilting resonances must not effectuate significant axial and radial displacements of the rotor.

Obviously, not all requirements can be fulfilled simultaneously, since they are partially conflicting. However, in the past several concepts have been developed that showed good performance in one or more of the beforementioned aspects.

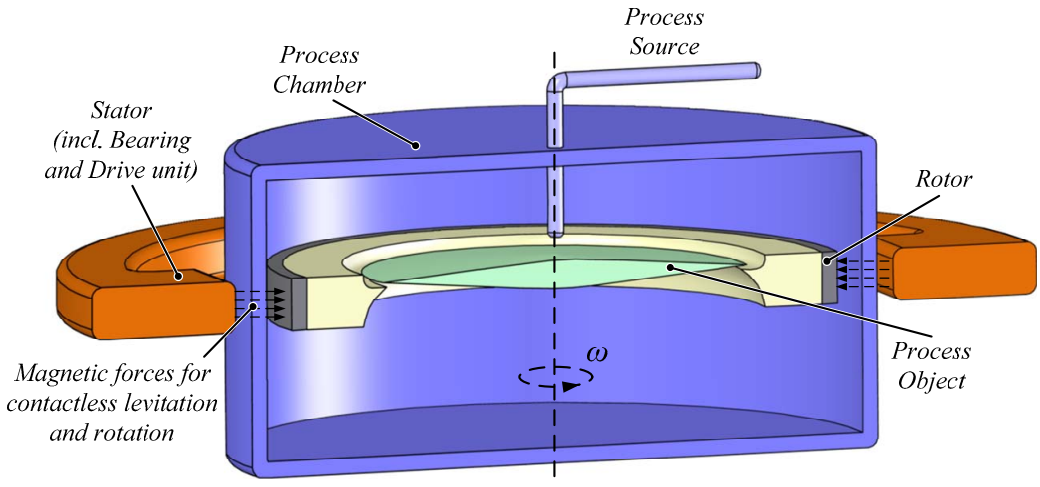

Fig. 1: Schematic cut view of an industry spinning process (e.g. coating, cleaning and polishing) that is hermetically sealed within a process chamber, using magnetic bearing technology for the levitation of the rotor.

In [13], a setup for a magnetically levitated pump system for use in semiconductor, chemical and pharmaceutical industry has been introduced. It incorporates a combined iron path for the drive and the bearing windings. Here, a high number of stator claws levitates and drives a single permanent magnet impeller, where its radial position is controlled actively and the axial position as well as the tilting around the radial axes is controlled passively. Due to the nature of the concept a very high number of stator claws would be necessary to levitate rotors with large diameters (i.e. number of pole pairs). Therefore, this concept has been adapted in pump applications with a pole pair number of one and impeller diameters smaller than 100 mm.

Another concept has been presented in [14] and [15]. The concept features the utilization of the permanent magnet field of the rotor on different height levels for the drive and the bearing. The rotor can be built in a very compact way; however, due to the operation principle this concept uses only the stray flux components for the driving of the rotor, which results in a relatively low motor torque and a poor acceleration performance.

The bearingless segment motor with a combined bearing and drive has been presented in [16] and shows very good acceleration behavior in combination with a compact setup. However, due to the coupled windings for bearing and drive the control of the motor gets very complicated. Additionally, the concept demands a higher number of sensors and for increased power electronics effort.

Standard shaft motors with applied bearingless method as presented in [4] and [17] demand a high constructional effort for the bearing and drive windings and hardly allow the hermetical encapsulation of the process object. These motors are increasingly used for flywheel, pump and compressor applications.

In this paper, a new "Magnetically Levitated 2-Level Motor (ML2M)" is proposed, combining the advantages of the before-mentioned concepts. The principle of the ML2M is explained in more detail in section II. In section III, the functionality of the magnetic bearing is introduced and analytical descriptions of stability are given. This is followed by a design procedure of the permanent magnet synchronous drive presented in section IV. Finally, the outstanding performance of the ML2M is proven by measurements on a laboratory prototype in section V.

II. Principle of the 2-Level Motor Concept

The ML2M concept introduced in this paper is based on the principle that the bearing and drive forces are applied on two different height levels (cf. Fig. 2). This enables a drive structure with significantly increased torque as compared to the concepts presented in [14] and [15]. In comparison to the motors with integrated drive/ bearing functionality [16] the proposed 2-level concept shows a greatly reduced control effort and the advantage of separately optimized drive and bearing system. Furthermore, the homopolar bearing of the ML2M allows very high rotational speeds, while for the concepts featuring a multipolar bearing [13], [16] the maximum rotational speed is limited by the current rise capabilities of the bearing and the time delays in the signal electronics.

A schematic cut view is depicted in Fig. 2. At the upper level, the magnetic bearing is located, consisting of rotor and stator permanent magnets (in order to provide a magnetic biasing) and the bearing windings around the four stator claws. The permanent magnet synchronous motor drive is positioned at an axially lower level. The

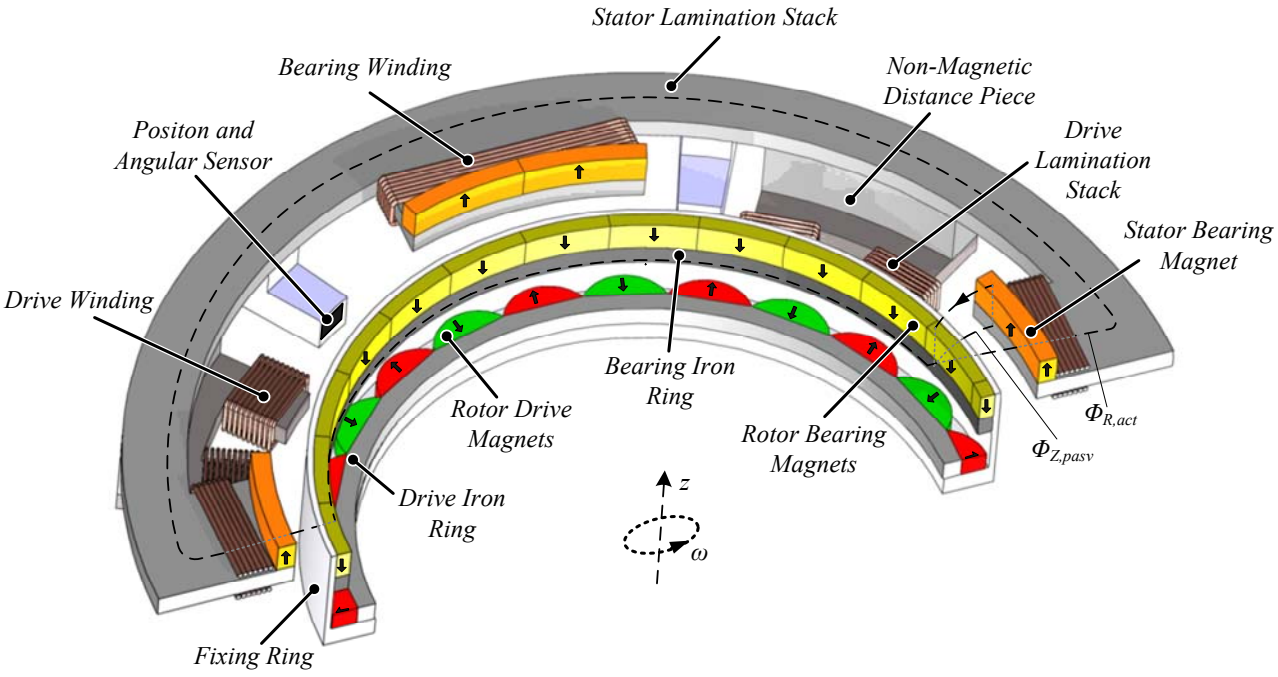

Fig. 2: Schematic cut view of the "Magnetically Levitated 2-Level Motor (ML2M)" including bearing and drive units on stator and rotor side. The flux path ($\Phi_{Z,pasv}$) of the passively generated force stabilizing the axial position and the tilting is indicated. The radial position is controlled actively and causes a flux ($\Phi_{R,act}$) through the stator lamination stack, which consequently causes a controlled radial force.

rotor magnets are round-shaped and have an alternate diametrical magnetization. Additionally, the drive claws and windings are located between the bearing claws on the stator, wherefore a more compact setup can be achieved. Position and angular sensors as introduced in [18] are distributed around the stator for the detection of the radial position and the rotation speed.

III. HOMOPOLAR MAGNETIC BEARING

A. Design

With the aid of the homopolar magnetic bearing the rotor of the ML2M is levitated in a contactless manner. The homopolar magnetic bearing consists of axially magnetized permanent magnets fixed on an iron ring on both the stator and the rotor side. The bearing magnets stabilize the axial position and the tilting through reluctance forces (cf. Fig. 3 and flux path $\Phi_{Z,pasv}$ in Fig. 2). However, this positive axial stabilization causes also a negative destabilization in radial direction [19]-[21] that has to be compensated actively. Therefore, the flux density in the air gap is altered with the aid of the bearing windings that are supplied with the bearing current I_D (see flux path $\Phi_{R,act}$ in Fig. 2). The rotor is then moved into the direction of the larger flux density.

The passive stabilization properties of the axial position and the tilting of the rotor through reluctance forces in the air gap are depicted in Fig. 3. An axial deflection of the rotor out of its force equilibrium position causes restoring forces, since the reluctance forces tend to minimize the magnetic resistance as depicted in Fig. 3(a). As the cross sectional area of the magnetic bearing and the material properties do not change, the only way to reach this minimum is the shortening of the length of the flux lines. Through this mechanism the rotor is brought back again into its force equilibrium position, which depends on the specific rotor construction and the rotor mass as will be explained later. At the same time, tilting is stabilized passively as depicted in Fig. 3(b). Here, the reluctance forces cause the stabilizing tilting torque $M_{tilt,st}$, which restores the rotor to be in line with the stator.

Besides the passive stabilization of the rotor, the permanent magnets also increase the effective flux density in the air gap, which serves as a biasing flux density for the active radial forces. Due to the quadratic relationship between the flux density and the radial force, this magnetic biasing effectively reduces the necessary bearing winding number N_B and the bearing current I_B in order to generate large radial forces for the radial stabilization of the rotor. Typically, the permanent magnet dimensions are designed in order to have the bias flux density in the range of half of the saturation flux density of the iron $B_{Sat,Fe}$. In this way, the bearing winding effort is greatly reduced for generating large forces and there is still a safety margin in order to avoid the saturation of the iron. However, for a stable levitation some more design aspects have to be considered. Therefore, in the following some crucial parameters that characterize the levitation properties are introduced and simple guidelines that have to be fulfilled are given.

Firstly, the axial stiffness $k_{Z,B}$ [N/mm] describes the axial force F_Z [N] that is needed in order to move the

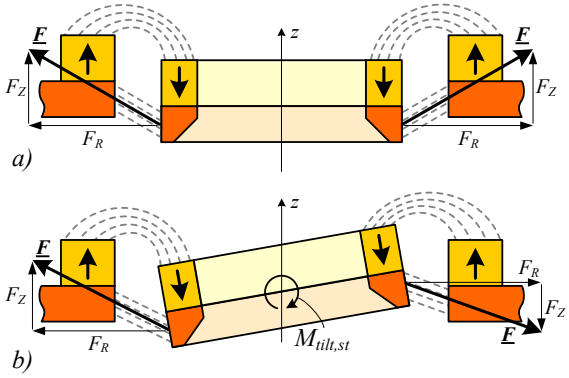

Fig. 3: Principle of the passive (a) axial and (b) tilting stabilization through reluctance forces for the axially magnetized permanent magnetic bearing of the ML2M.

rotor $z = 1$ mm out of its stable position [22]. Secondly, the non-linear radial stiffness $k_{R,B}$ [N/mm] specifies the required radial force F_R [N] needed to return the rotor back to its stable position after being displaced by 1 mm. As mentioned before the permanent magnets on both the stator and the rotor bearing iron ring are used for flux biasing and to define the flux path through the air gap. The flux density can be altered depending on the rotor position by supplying the bearing windings with bearing currents, thereby generating Maxwell-forces towards the target position [23]. The current imposed flux path $\Phi_{R,act}$ of two opposing bearing claws causes the actively controlled radial force, which is depicted in Fig. 2. And thirdly, the force-current factor $k_{I,B}$ [N/(A·turns)] describes the force that can be generated per ampere-turn in the bearing winding.

Generally, a high axial stiffness $k_{Z,B}$ is desired in order to counteract the weight force

$$k_{Z,B} \cdot \Delta z = m \cdot g \tag{1}$$

resulting in a minimum axial stiffness

$$k_{Z,B} > \frac{m \cdot g}{\Delta z_{\max}}, \tag{2}$$

where Δz_{max} is the maximum allowable displacement in the axial direction, m is the mass of the rotor and g is the gravitational constant.

However, as mentioned before, a high axial stiffness comes along with a destabilizing radial stiffness that has to be overcome by the stabilizing active magnetic force imposed by the bearing currents. Therefore, for allowing a maximum radial deflection Δr_{max} from the stable position, the force-current factor $k_{I,B}$ has to be larger than a minimum value given by

$$k_{I,B} > \frac{k_{R,B} \cdot \Delta r_{\max}}{N_B \cdot I_B}, \tag{3}$$

where N_B is the bearing coil winding number and I_B the bearing controller current. Here, it has to be considered that the force-displacement dependency is non-linear; therefore, evaluating (3) with a linear radial stiffness $k_{R,B}$ is only valid within a limited operating range.

In order to facilitate the fulfillment of (3), N_B has to be chosen as high as possible. However, a high number of bearing turns decreases the current rise capability in the bearing inductance L_B. The electrical time constant

τ_E of the bearing is given by

$$\tau_E = \frac{I_{B,\max} \cdot L_B}{U_{DC}}, \tag{4}$$

where $I_{B,max}$ is the maximum bearing current and U_{DC} the dc link voltage of an inverter in full bridge configuration driving the bearing coil. Since L_B scales with N_B^2, the electrical time constant τ_E increases quadratically with N_B. For achieving a stable system control the condition

$$\tau_E << \tau_M, \tag{5}$$

with the mechanical time constant τ_M defined as

$$\tau_M = \sqrt{\frac{m}{k_{R,B}}}, \tag{6}$$

has to be satisfied, i.e. a small number of bearing windings is desirable from this point of view. Therefore, the selection of N_B will always be a trade-off between high dynamics (cf. (4) and (5)) and the maximum force condition (cf. (3)) as was also stated in [24].

B. Interference with the drive system

Due to the axial and circumferential separation of the drive and bearing system the mutual coupling effects can be assumed to be low. However, in addition to the bearing's radial stiffness $k_{R,B}$, the diametrically magnetized permanent magnets of the drive on the rotor cause a magnetic force towards the stator leading to an additional stabilizing axial stiffness $k_{Z,D}$ and a destabilizing radial stiffness $k_{R,D}$. These stiffness parameters have to be considered and added into the bearing design formulas presented in (1) – (3).

Additionally, interactions between the bearing and the drive unit may cause tilting problems, which have to be considered and are addressed here now shortly. The tilting mechanisms are schematically depicted in Fig. 4 for a rotor, which is tilted around the bearing axis. The destabilizing radial force $F_{R,D}$ of the drive causes a tilting torque $M_{R,D}$ around the bearing axis center with the distance h between the bearing and the drive being the lever

$$M_{R,D} = F_{R,D} \cdot h. \tag{7}$$

The radial destabilizing force caused by the drive can be described by

$$F_{R,D} = k_{R,D} \cdot h \cdot \alpha_{tilt}, \tag{8}$$

where α_{tilt} is the tilting angle. At the same time the rotor is stabilized through the stabilizing torque $M_{Z,B}$ defined as

$$M_{Z,B} = F_\alpha \cdot r \tag{9}$$

with the restoring passive tilting force F_α acting on the radius of the rotor r as the lever. The tilting force F_α can be calculated out of the axial bearing stiffness $k_{Z,B}$ with

$$F_\alpha = k_\alpha \cdot \alpha_{Tilt} = k_{Z,B} \cdot f_a(\varphi_B) \cdot \alpha_{Tilt} \cdot r. \tag{10}$$

with k_α [N/rad] being the tilting stiffness and f_α being a weighting factor depending on the bearing claw opening angle φ_B (cf. Fig. 6). This factor summarizes the different contributions of the four bearing units at the stator in dependency on φ_B for a tilting situation around a certain radial axis. For practically reasonable bearing claw opening angles in the range of $\varphi_B = 25\ldots60°$mech. this

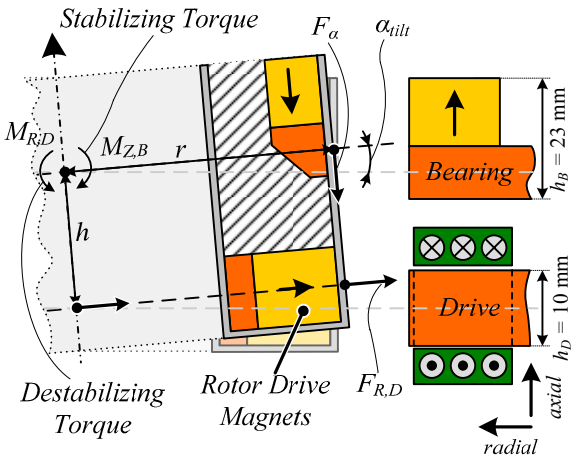

Fig. 4: Schematic cut view of the tilted ML2M rotor with radial stabilizing torque $M_{Z,B}$ and destabilizing torque $M_{R,D}$ indicated.

factor is approximately $f_\alpha \approx 0.5$ rad^{-1}. This proportion factor can be interpreted such that in total two of the four bearing claws contribute to the restoring tilting force F_α. With this, a tilting tendency factor ξ_{tilt} of the ML2M can be described as the ratio of the two torque values by

$$\xi_{tilt} = \frac{M_{R,D}}{M_{Z,B}} = 2 \cdot \frac{k_{R,D} \cdot h^2}{k_{Z,B} \cdot r^2}. \tag{11}$$

In order to guarantee a stable operation the condition $\xi_{tilt} << 1$ has to be ensured. Usually, this is the case for rotors with a large radius to height ratio, as this is the case for the setup at hand.

An additional destabilizing torque on the drive level may be caused by the superimposed electromagnetic forces resulting from the drive winding currents. However, as will be shown in following section, for the presented ML2M drive the opening angle of the drive lamination stack φ_D is selected equal to the angle of 180°el. With this, there will always be the same amount of attracting and repellent radial forces caused by the drive ampere-turns for any rotor position. Therefore, no resulting radial force acting on the rotor is caused by the drive current, which is why it is not considered in (11).

IV. Permanent Magnet Synchronous Drive

A. Basics

The main components of the 2-phase permanent magnet synchronous drive [25] are depicted schematically in Fig. 5. The flux path is defined by the stator drive claws with the drive windings, the air gap and the drive magnets located on the rotor drive magnet ring. The drive magnets are round-shaped and with alternate diametrical magnetization in order to generate a sinusoidal-like flux density distribution in the air gap. A motor torque M_D is generated if the drive windings are supplied with an appropriate drive current I_D, resulting in a tangential force F_T. Since permanent magnets always attract iron independently of their magnetization direction, the drive has priority positions. These priority positions are defined by the constructive design (φ_D, w_{Claw}, d_{Claw}) of the stator drive claw with respect to the rotor magnet dimensions,

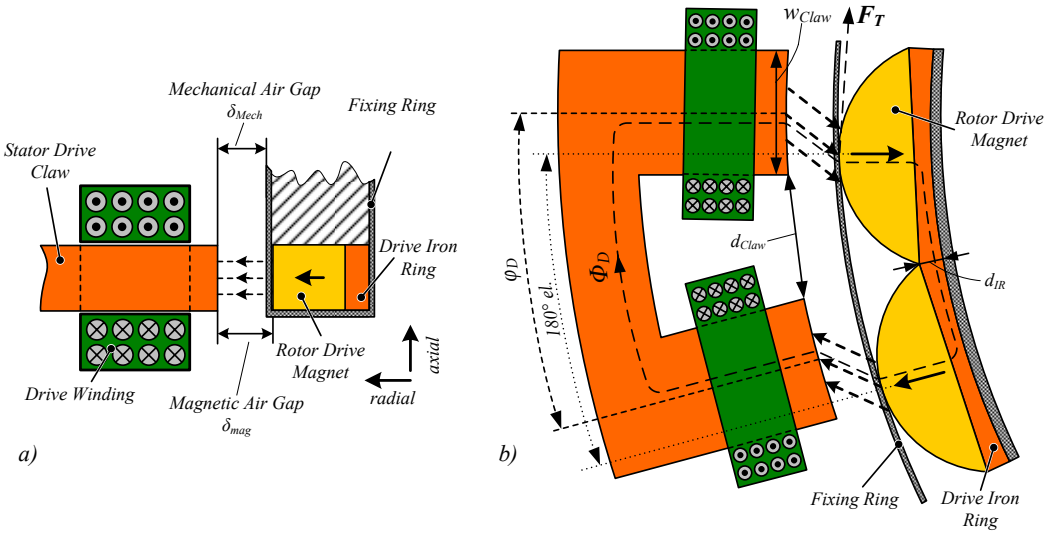

Fig. 5: Principle of the drive of the Novel Magnetically Levitated 2-Level Motor with side view (a) and top view (b).

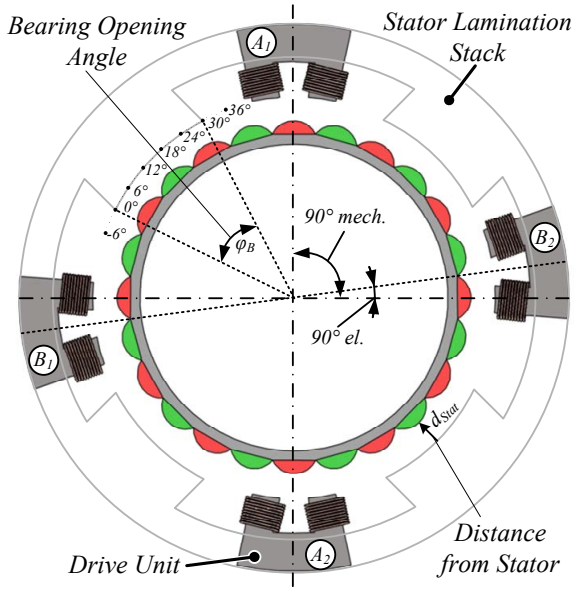

Fig. 6: Schematic top view of the ML2Ms 2-phase drive unit with 90°el. shifted drive axes in order to reduce the cogging torque $M_{Cogging}$ and generate a constant drive torque M_D. Additionally, the discrete angular positions along the bearing claw are indicated as referenced in Fig. 12.

the rotor magnet strength as well as the size of the air gap δ_{Mag}. This behavior causes a cogging torque $M_{Cogging}$, which induces additional losses and can lead to vibrations and jerky rotation especially in the low rotational speed range [26]. The cogging torque of the 2-phase drive of the ML2M can be greatly reduced, if the two drive axes are shifted by additional 90°el. as depicted in Fig. 6. This avoids having two maximum field densities forcing the rotor into a preferred position. A further reduction of the cogging torque $M_{Cogging}$ can be achieved by an optimization of the stator claw dimensions (see section IV.B). Additionally, the phase shift of the drive phases by 90°el. results in a constant motor drive torque M_D that is independent of the rotor angular position [27] as depicted in Fig. 7. Assuming sinusoidal waveforms, the absence of magnetic saturation and the employment of field oriented control, the torque is given by

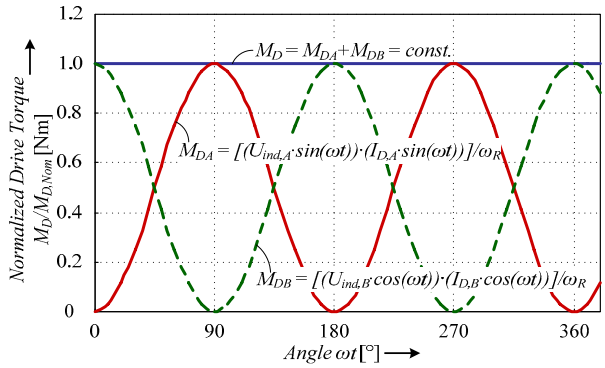

Fig. 7: Visualization of the constant motor torque M_D generation through the deployment of two by 90°el. shifted drive phases M_{DA} and M_{DB}.

$$M_D = \frac{U_{ind}(\omega t) \cdot I_D(\omega t)}{\omega_R} \tag{12}$$

with the speed dependent induced voltage U_{ind}, the drive current I_D, which is controlled to be in phase with U_{ind}, the angular mechanical rotation speed ω_R and the angular electrical frequency ω. Due to the field-orientated control the drive current and the induced voltage are in phase and thus the drive torque M_{DA} in phase A is a square sine and the drive torque M_{DB} of the electrically 90° phase shifted phase B is a square cosine. With

$$\cos^2(\omega t) + \sin^2(\omega t) = 1 \tag{13}$$

a constant motor torque M_D results from the superposition of the two single phase torques that have the same absolute value.

The main drive parameters introduced depend mainly on the flux density distribution in the air gap. Since this distribution is highly non-linear and it is inexpedient to describe them analytically the subsequent design considerations are carried out based on 3D finite element simulations by using Maxwell® 3D [28].

B. Design

The major degrees of freedom for the permanent magnet synchronous drive design are the shape of the stator claws, especially the drive stator claw width w_{Claw}, the number of turns N_D of the drive coils and the thick-

ness d_{IR} of the drive iron ring. By optimizing these parameters the design aim of minimum cogging torque $M_{Cogging}$, acceptable radial stiffness $k_{R,D}$ and maximum motor torque M_D can be achieved.

A first great reduction of the cogging torque can already be achieved, if the drive phase axes are circularly shifted by 90°el. as mentioned in the previous. For simplifying the design simple U-shaped drive elements as depicted in Fig. 5(b) are considered here. As a detailed analysis shows, this shape is not optimal regarding the cogging torque, but has much smaller saturation affinity as has been shown in [29], which is important for high acceleration motors with large air gap as this is the case here. Since the cogging torque does not reach critical values due to the before-mentioned 90°el. shifting of the phase axes, this shape is considered here. Furthermore, the opening angle φ_D is set to φ_D = 180°el. This maximizes the achievable torque and leaves w_{Claw} as the only dimensional optimization parameter. Fig. 8 shows the simulation results of $M_{Cogging}$, M_D and $k_{R,D}$ for different stator claw widths w_{Claw}. As can be seen there, a minimum cogging torque is reached for w_{Claw} = 20 mm at a high motor torque. Furthermore, Fig. 8 shows the linear dependency of the negative radial stiffness on the stator claw widths, which justifies the selection of w_{Claw} = 20 mm rather than any wider stator claw.

Another design parameter is the thickness d_{IR} of the drive iron ring, which constitutes the feedback path for the drive flux Φ_D. If d_{IR} is selected very small, saturation effects in the drive iron ring will occur and will degrade the flux density in the air gap and consequently the induced voltage and the drive torque. The critical thickness for d_{IR} is given at the connection point between two rotor magnets, since the maximum drive flux has to pass through there (cf. Fig. 5). The resulting flux density defining the saturation in the iron ring is composed of two flux components, where the major component is the permanent flux density by the drive permanent magnets and the minor component is the flux imposed by the drive winding currents. The distance between two stator claws d_{Claw} is typically much smaller than the magnetic air gap δ_{Mag} plus the length of the permanent magnets l_{PM} that add on to the flux path due

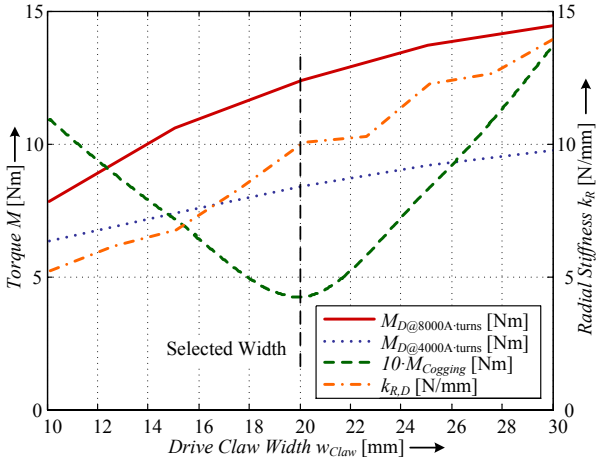

Fig. 8: Results of 3D finite element simulations for the cogging torque $M_{Cogging}$, the radial stiffness $k_{R,D}$ and the motor drive torque M_D for two different ampere-turn ratios (per drive claw) in dependency on the stator claw width w_{Claw}.

permanent magnets l_{PM} that add on to the flux path due to there air like permeability ($\mu_{Mag} \approx 1$, cf. Fig. 9). Therefore, the current generated flux will mainly pass through the space between the stator claws and hardly enter the rotor iron ring. Hence, the flux density in the iron ring will be clearly dominated by the permanent magnets. Thus, only this portion will be considered for the following design guidelines.

An integration of the approximately sinusoidal flux density distribution along the back side of half a drive magnet (cf. Fig. 9) gives the total flux Φ_D that passes from one magnet to the neighbored one through the iron ring and is defined by

$$\Phi_D = \int_{A_{PM}} B \cdot dA_{PM} = \int_0^{r\pi/2p} B_{PM} \cdot \sin\left(\frac{b \cdot p}{r_{IR}}\right) \cdot h \cdot db = \frac{B_{PM} \cdot r_{IR} \cdot h_{IR}}{p} \tag{14}$$

with the arc length b (cf. Fig. 9), the permanent magnet flux density B_{PM} passing perpendicularly through the back side area A_{PM} of the magnet (cf. Fig. 9), the inner drive iron ring radius r_{IR}, the iron ring height h_{IR} and the number of pole pairs p.

In order not to saturate the iron material ($B_{PM} < B_{Sat,Fe}$) for a worst case situation ($\Phi_D = \Phi_{D,max}$) at the position b = 0 rad the cross-section A_Φ has to fulfill the condition

$$A_\Phi \geq \frac{\Phi_{D,\max}}{B_{Sat,Fe}}, \tag{15}$$

which gives with $A_\Phi = h_{IR} \cdot d_{IR}$ (cf. Fig. 9) the minimum thickness for the drive iron ring

$$d_{IR} \geq \frac{B_{PM,\max} \cdot r_{IR}}{B_{Sat,Fe} \cdot p}. \tag{16}$$

where $B_{PM,max}$ is the maximum appearing value of B_{PM}. The exact value of the flux density B_{PM} can be ascertained only by electromagnetic simulations. However, analytical approximations can already give a rough guideline. The maximum value of the flux density $B_{PM,max}$, which represents the worst-case condition for the saturation in the iron, occurs, when the air gap between rotor and stator becomes minimal, i.e. when the rotor magnets lie exactly in front of the drive claws as shown in Fig. 9. In this position, the flux density can be estimated (with $\mu_R \to \infty$) by

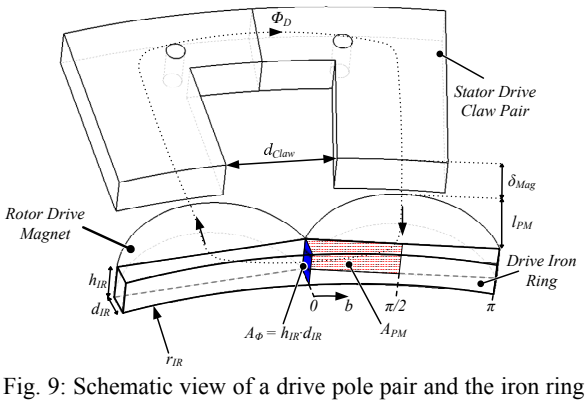

Fig. 9: Schematic view of a drive pole pair and the iron ring in front of a stator claw pair with flux cross section areas indicated.

$$B_{PM,\max} \le B_R \cdot \frac{l_{PM}}{l_{PM} + \delta_{mag}}, \qquad (17)$$

where B_R is the remanence flux density of the permanent magnet, l_{PM} is the length of a permanent magnet, and δ_{Mag} is the magnetic air gap (including the thickness of the fixing ring). Since in reality not all lines of the magnetic flux will follow the shortest way (and some not even enter the stator claw) and thus the average air gap will be larger than δ_{Mag}, (17) represents a worst-case approximation. As a detailed analysis shows, at that considered maximum point the impressed force by the drive windings is zero, therefore the before-mentioned negligence of that influence has been correct.

Hence, (16) and (17) provide a guideline for the required iron thickness d_{IR} in dependency of the pole pair number p and the radius r. However, selecting d_{IR} smaller than given in (16) relates to a weight reduction and can probably lead to an increased acceleration performance of the motor even though the air gap flux density is reduced.

Besides the discussed constructional parameters the winding number of the drive coils greatly influences the acceleration behavior of the ML2M. According to [14] the maximum applicable drive current $\hat{I}_D$ per phase is given by

$$\hat{I}_D = \frac{-\hat{U}_{ind} \cdot R_D \pm \sqrt{(R_D^2 + \omega^2 \cdot L_D^2)\, U_{DC}^2 - \omega^2 \cdot L_D^2 \cdot \hat{U}_{ind}^2}}{R_D^2 + \omega^2 \cdot L_D^2}, \qquad (18)$$

where $\hat{U}_{ind}$ is the rotation speed dependent induced voltage amplitude, R_D is the winding resistance per phase, L_D the drive winding inductance per phase and $\omega = 2\pi \cdot n_R \cdot p/60$ the electrical angular frequency with n_R being the rotational speed in rotations per minute.

As can be seen in Fig. 10(a), for low rotational speeds the drive current is limited by the maximum current $I_{PE,max}$ provided by the power electronics, while for higher rotation speeds the current is decreasing due to the growing impedance $\omega \cdot L_D$ and due to the induced voltage which is increasing linearly with ω (cf. Fig. 10(a)). Both $U_{ind} \sim N_D$ and $L_D \sim N_D^2$ are depending on the number of coil turns N_D, wherefore the available drive current is decreasing with increasing turns number (cf. Fig. 10(a)). On the other hand, the drive power per phase is given by the product of the induced voltage and the drive current

$$P_D = U_{ind}(N_D) \cdot I_D(N_D). \qquad (19)$$

Thus, an optimum number of turns can be identified for a certain rotation speed region. This is shown in Fig. 10(b), where the acceleration times for different rotor speeds and winding numbers for a 2-phase drive are plotted. It shows that a target rotational speed of 2000 rpm can be reached within 3.6 s for an optimum number of turns of N_D = 600 per phase. It has to be mentioned that this calculation is only correct for non-saturated material both in the stator claws and in the iron ring as discussed before and for sinusoidal current and induced voltage waveforms being perfectly in phase (due to field oriented control).

V. Experimental Performance

Based on the design guidelines that have been presented in the previous sections, a prototype has been built in order to verify the design considerations. In Table 1 the characteristic parameters of the chosen design are compiled. Fig. 11 shows the complete assembly including the rotor and the stator-sided bearing and drive system. The axial bearing stiffness $k_{Z,B}$ and the rotor mass m result in a gravitational axial displacement $z_{defl,grav}$ of approximately 2 mm. Compared to the considerably larger active bearing height h_B = 23 mm (cf. Fig. 4) this displacement has no significant influence on the magnetic levitation system.

A 3D plot of the measured flux densities in the axial level of the bearing stator lamination stack within the air gap along the bearing claw is shown in Fig. 12, whereby the discrete angular positions along the bearing claw are corresponding with the indications in the schematic top view of Fig. 6. The 3D plot shows flux density values in the air gap in the range of about of $B_{Air} \approx 200\ldots250$ mT in front of the bearing claw. In close proximity to the bearing magnets on rotor and stator side the flux density is increased due to self closing flux lines. Distinct flux density peaks can be observed on the edges of the stator magnets resulting from edge shortcut effects. Due to the large air gap, the flux density values are comparatively low, since bias flux densities in the range of half of the

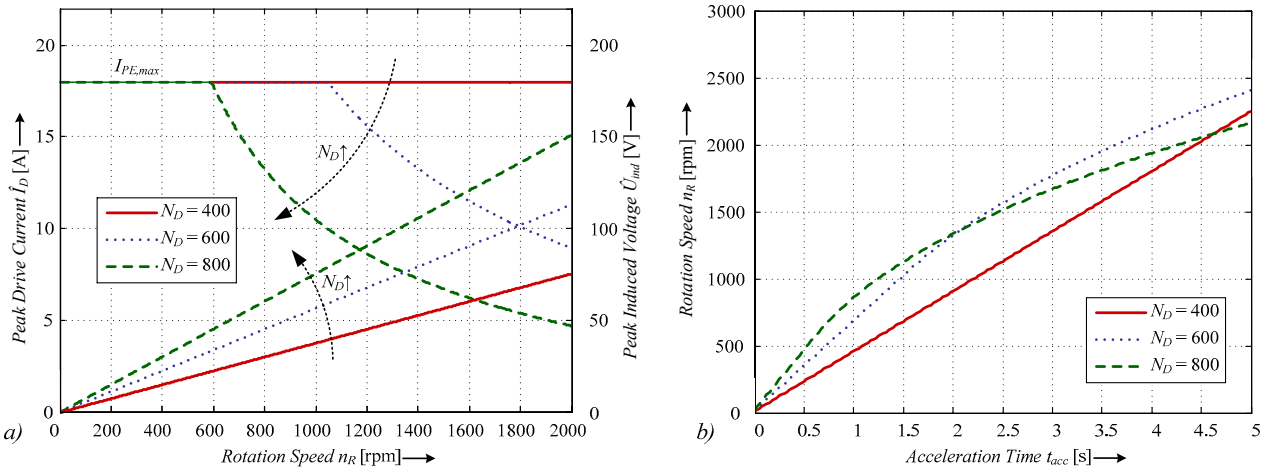

Fig. 10: (a) Achievable drive current $\hat{I}_D$ (for $I_{PE,\,max}$ = 18 A) and induced voltage $\hat{U}_{ind}$ in dependency of the rotation speed n_R for different drive winding numbers N_D and (b) estimated acceleration performance of the 2-phase ML2M.

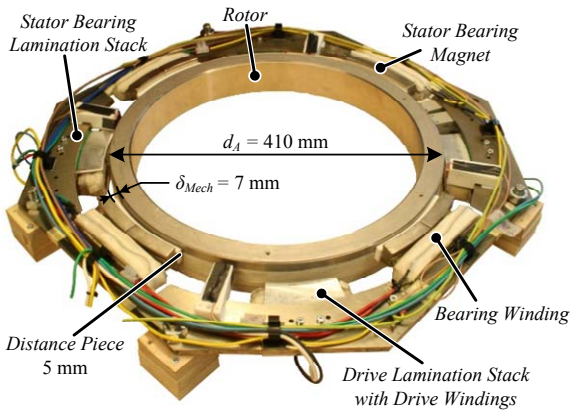

Fig. 11: Photography of completely assembled laboratory prototype with bearing and drive windings and geometry parameters outside rotor diameter d_A and mechanical air gap δ_{Mech} indicated.

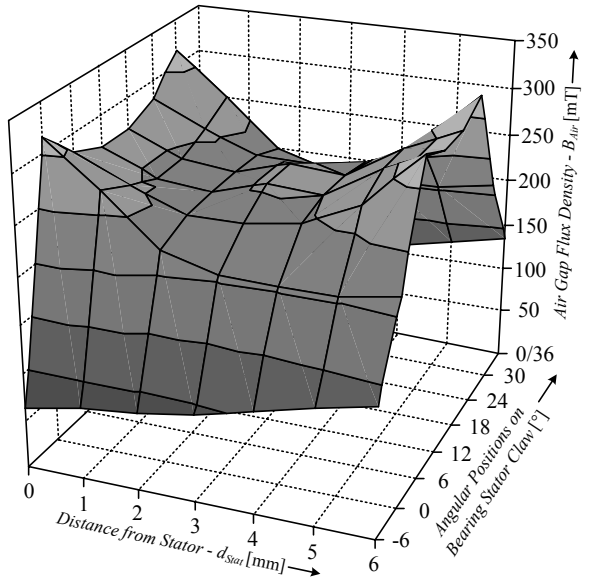

Fig. 12: 3D plot of the flux density in the air gap along the stator circumference in dependency of the distance from the stator. The bearing angle positions are indicated in Fig. 6.

saturation flux density of the iron would be desirable as mentioned already in section III.A. However, for this air gap length, higher bias flux densities could only be achieved by significantly larger bearing unit dimensions (both permanent magnets and iron), which would result in a less compact setup.

In order to prove the applicability of the 3D FEM simulations the measured values of the axial and radial stiffness and the force-current factor are compared in Fig. 13(a)-(c) with the simulated values and show generally a good agreement. For the axial stiffness (cf. Fig. 13(a)) the assumption of a linear factor $k_{Z,B}$ is correct in a wide area. For the measurement of the axial stiffness a force meter was attached to the mechanically centered rotor. The axial deflection Δz resulting from the applied axial force F_Z was then measured with the aid of laser distance sensors. Due to the square dependency of the radial force on the displacement, the radial stiffness (cf. Fig. 13(b)) has been approximated with a quadratic fit function. For the measurement the rotor was mechanically deflected from the centre position along one

TABLE 1: DESIGN DATA OF THE EXPERIMENTAL SETUP

Outside rotor diameter d_A	410 mm
Mechanical air gap δ_{Mech}	7 mm
Maximum Radial Deflection Δr_{max}	2 mm
Number of pole pairs p	12
Axial stiffness $k_{Z,B}$	25 N/mm
Radial stiffness $k_{R,B}$	-20 N/mm
Force-Current factor $k_{I,B}$	1 N/(100 A·turns)
Tilting stiffness $k_{\varphi,B}$	57 N/rad
Motor Torque M_D for I_D = 1Arms	0.7 Nm
Cogging Torque $M_{Cogging}$	0.45 Nm
Bearing phase winding number N_B	2 x 300 turns
Drive phase winding number N_D	4 x 150 turns
Rotor mass m	5 kg
Drive Iron Ring Thickness d_{IR}	6 mm
Drive Iron Ring Height h_{IR}	10 mm
Stator Claw Width w_{Claw}	20 mm
Drive Opening Angle φ_D	180°el.
Bearing Opening Angle φ_B	360°el.
Drive Height h_D	10 mm
Bearing Height h_B	23 mm

bearing axis by distance pieces, while the rotor was mechanically centered in the other bearing axis. The force needed to bring the rotor back into the center position was then measured using a force meter. The small deviations between the measured radial stiffness and the values predicted by the simulations can be related to the impreciseness of the measurement method. The match of simulation and measurement data is still acceptable. For the force-current factor, a perfect agreement between measurement and simulations can be seen in Fig. 13(c). For the measurement, the rotor was levitated and a force was applied with a force meter in one bearing axis. The appearing current was measured and used for the calculation of the force-current factor.

Besides the static properties of the magnetic bearing, in the following also the dynamics are investigated in order to describe the suspension characteristics completely. The deflection of the rotor is controlled by a cascaded controller, with the position controller in the outer loop and the bearing current controller in the inner loop. The control structure is not explained here for the sake of brevity, but can be found e.g. in [30]. For the characterization of the bearing current controller a step response of the bearing current I_B for a 10 A step of the bearing current reference $I_{B,ref}$ is shown in Fig. 14. The evaluated electrical time constant τ_E = 1.56 ms clearly fulfils the condition formulated in (5), since it is much smaller than the mechanical time constant τ_M = 15.8 ms, which can be calculated from (6) and the design data given in Table 1.

The step response of the deflection in y-axis y_{defl} for a 650 µm step of the position controller reference signal POS_{ref} is shown in Fig. 15. The maximum radial deflection is limited mechanically to Δr_{max} = 2 mm by

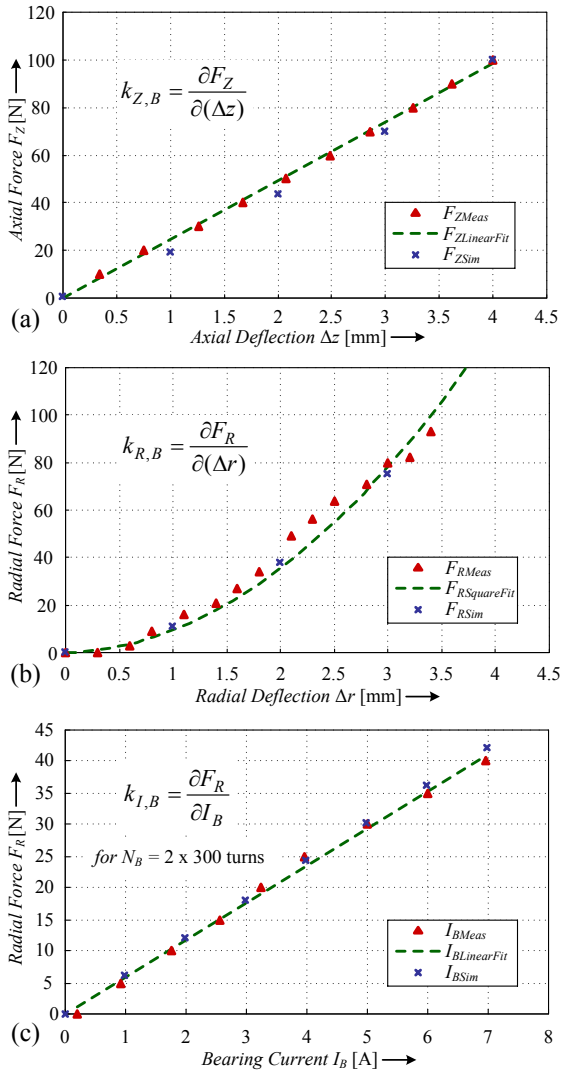

Fig. 13: (a) Measured and simulated axial stiffness; (b) measured and simulated radial stiffness; and (c) measured and simulated force-current factor.

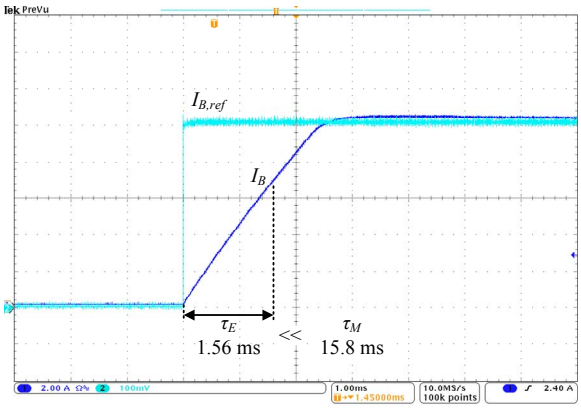

Fig. 14: Step response of the bearing current I_B for a 10 A step of the bearing current reference $I_{B,ref}$ with the electrical time constant τ_E indicated and compared to the mechanical time constant τ_M (scale: 2 A/div, 1 ms/div.).

distances pieces as indicated in Fig. 11. Therefore, the 650 µm step corresponds to a 32% change within the operating range, leading to an overshoot of 27% and a settle time of 160 ms. The radial deflection of the rotor y_{defl} during acceleration from 0 to 2000 rpm is shown

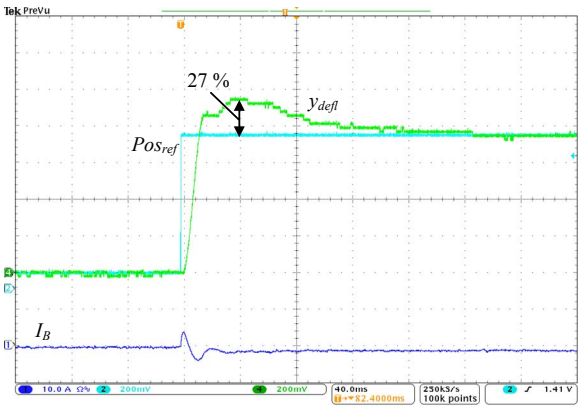

Fig. 15: Step response of the radial deflection in y-axis y_{defl} for a 650 µm step of the position controller reference signal POS_{ref} with a 27% overshoot indicated and the corresponding bearing current I_B (scales: 10 A/div., 170 µm/div., 40 ms/div.).

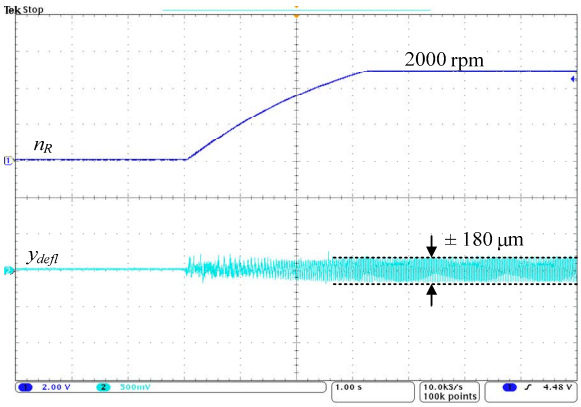

Fig. 16: Radial deflection of the rotor in y-axis during acceleration from 0 to 2000 rpm measured with laser distance sensors (scales: 800 rpm/div., 500 µm/div., 1 s/ div.).

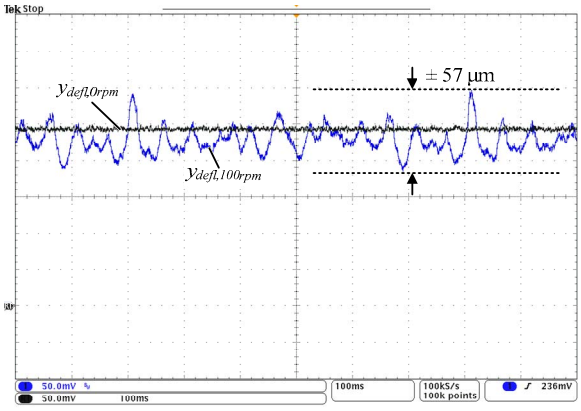

Fig. 17: Influence of rotor rotation on the radial positioning at 0 rpm $y_{defl,0rpm}$ compared to 100 rpm $y_{defl,100rpm}$ (scales: 50 µm/div., 100 ms/div.).

in Fig. 16. Here, the maximum occurring radial deflection is in the range of $y_{defl} = \pm$ 180 µm. This deflection is acceptable and is mainly caused by asymmetries of the rotor prototype that cause rotational unbalances, which could be eliminated by more advanced control schemes. The impact of rotation on the radial deflection of the rotor is demonstrated in Fig. 17 exemplarily for 100 rpm. Here, the rotor has virtually no radial deflection if in standstill $y_{defl,0rpm} \approx 0$. If the motor rotates at 100 rpm, the radial deflection increases up to $y_{defl,100rpm} = \pm$ 57 µm. Although the radial deflection values are small and in an

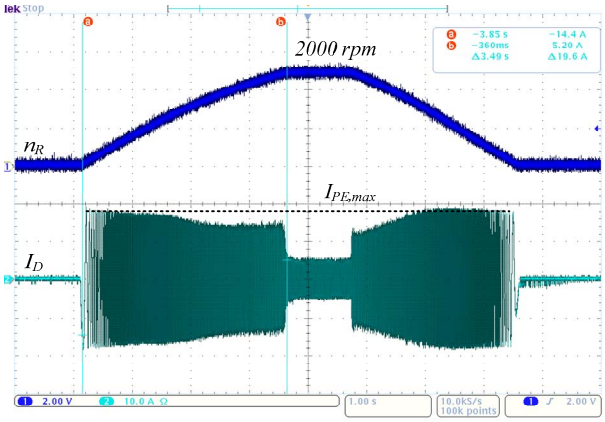

Fig. 18: Acceleration performance of ML2M from 0 to 2000 rpm for $I_{PE,max}$ = 18A in 3.5s and deceleration in 2.8s (scales: 800 rpm/div., 10 A/div., 1 s/div.).

acceptable range already, they can be reduced by using more precise fabrication methods for the rotor for future prototypes and/or by control schemes with an unbalance compensation circuit.

Finally, Fig. 18 shows the acceleration performance of the ML2M drive from 0 rpm to 2000 rpm for $\hat{I}_{PE,max}$ = 18 A. For the run-up sequence, the final speed of 2000 rpm can be reached within 3.8 s, which is close to the value predicted by the simulations (cf. section IV.B), while the deceleration is accomplished within 2.8 s. This performance is very satisfactory considering the motor dimensions and the large air gap. With this, on the one hand the design procedure and correctness of the simulations could be verified, and on the other hand the excellent performance of the ML2M concept could be proved.

VI. CONCLUSIONS

The paper describes a new concept called "Novel Magnetically Levitated 2-Level Motor" (ML2M) that is of high interest for several industry branches, where contactless levitation and rotation in clean room environments is required. The new concept features high acceleration capability, a compact setup, low power electronics effort and a separate design and simple control of the bearing and drive units even for large air gaps. In this paper, the functionality of the ML2M concept has been explained and guidelines for the design of the drive and bearing unit have been presented, also taking saturation and coupling effects between the drive and bearing system into account. Finally, the theoretical considerations have been verified on a prototype setup by extensive measurements of design parameters, performance values, and achievable acceleration times.

REFERENCES

[1] R. Schoeb, N. Barletta, "Principle and Application of a Bearingless Slice Motor," *JSME Int. Journal Series C*, pp.593-598, 1997.

[2] A. Chiba, D.T. Power, M.A Rahman, "Chracteristics of a Bearingless Induction Motor," *IEEE Trans. Magnetics*, vol. 27, no. 6, Nov. 1991.

[3] S. Silber, W. Amrhein, P. Boesch, R. Schoeb, N. Barletta, "Design aspects of bearingless slice motors," *IEEE/ASME Trans. Mechatronics,* vol. 10, no.6, pp.611-617, Dec. 2005.

[4] A.O. Salazar, R.M. Stephan, "A bearingless method for induction machines," *IEEE Trans. on Magnetics*, vol.29, no.6, pp.2965-2967, Nov. 1993.

[5] H. Kusayanagi, M. Takemoto, Y. Tanaka, A. Chiba, T. Fukao, "Basic characteristics of a permanent-magnet type bearingless motor with positive salient pole," *ICEMS. International Conference on Electrical Machines and Systems*, pp.1698-1703, 8-11 Oct. 2007.

[6] N. Watanabe, H. Sugimoto, A. Chiba, T. Fukao, M. Takemoto, "Basic Characteristic of the Multi-Consequent-Pole Bearingless Motor," *Power Conversion Conference - Nagoya, 2007. PCC '07*, pp.1565-1570, 2-5 Apr. 2007.

[7] I.Y. Oenel, M.E.H. Benbouzid, "Induction Motor Bearing Failure Detection and Diagnosis: Park and Concordia Transform Approaches Comparative Study," *IEEE/ASME Transactions on Mechatronics*, vol.13, no.2, pp.257-262, Apr. 2008.

[8] M.N. Sahinkaya, A.-H.G. Abulrub, P.S. Keogh; C.R. Burrows, "Multiple Sliding and Rolling Contact Dynamics for a Flexible Rotor/Magnetic Bearing System," *IEEE/ASME Transactions on Mechatronics*, vol.12, no.2, pp.179-189, Apr. 2007.

[9] J. Boehm, R. Gerber, J.R. Hartley, S. Whitley, "Development of active magnetic bearings for high speed rotors," *IEEE Trans. on Magnetics*, vol.26, no.5, pp.2544-2546, Sep. 1990.

[10] A. Chiba, T. Fukao, M.A. Rahman, "Vibration Suppression of a Flexible Shaft with a Simplified Bearingless Induction Motor Drive," *Conference Record of the 2006 IEEE Industry Applications Conference, 41st IAS Annual Meeting*, vol.2, pp.836-842, 8-12 Oct. 2006.

[11] A. Wu, Z. Cai, M.S. de Queiroz, "Model-Based Control of Active Tilting-Pad Bearings," *IEEE/ASME Transactions on Mechatronics*, vol.12, no.6, pp.689-695, Dec. 2007.

[12] Y. Chisti, M. Moo-Young, "Clean-in-place systems for industrial bioreactors: Design, validation and operation," *Journal of Industrial Microbiology and Biotechnology*, 1994.

[13] N. Barletta, R. Schöb, "Design of a Bearingless Blood Pump," *3rd Int. Symp. on Magnetic Suspension Technology*, Tallahassee, 1995.

[14] R. Schoeb, N. Barletta, M. Weber and R. von Rohr, "Design of a Bearingless Bubble Bed Reactor", *Proc. 6th Int. Symp. on Magnetic Bearings*, pp.507–516., 1998.

[15] T. Schneeberger, J. W. Kolar, "Novel Integrated Bearingless Hollow-Shaft Drive," *Proc. of the IEEE Ind. Applic. Conf. IAS*, Tampa (USA), 8 – 12 Oct. 2006.

[16] W. Gruber, W. Amrhein, "Design of a Bearingless Segment Motor," *Proc. of the 10th Int. Symp. on Magnetic Bearings*, Martigny, 2006.

[17] K. Asami, A. Chiba, M.A. Rahman, T. Hoshino, A. Nakajima, "Stiffness analysis of a magnetically suspended bearingless motor with permanent magnet passive positioning," *IEEE Trans. on Magnetics*, vol.41, no.10, pp.3820-3822, Oct. 2005.

[18] J. Boehm; R. Gerber, N.R.C. Kiley, "Sensors for magnetic bearings," *IEEE Trans. on Magnetics*, vol.29, no.6, pp.2962-2964, Nov. 1993.

[19] J. Delamare, E. Rulliere, J.P. Yonnet, "Classification and synthesis of permanent magnet bearing configurations," *IEEE Trans. on Magnetics*, vol.31, no.6, pp.4190-4192, Nov. 1995.

[20] J.-P. Yonnet, "Permanent magnet bearings and couplings," *IEEE Trans. Magnetics*, vol.17, no.1, pp.1169- 1173, Jan. 1981.

[21] S. Earnshaw, "On the nature of the molecular forces which regulate the constitution of the luminiferous ether," *Trans. Camb. Phil. SOC.*, vol. 7, no. 1, pp.97-112, 1839.

[22] G. Stumberger, D. Dolinar, U. Palmer, K. Hameyer, "Optimization of radial active magnetic bearings using the finite element technique and the differential evolution algorithm," *IEEE Trans. on Magnetics*, vol.36, no.4, pp.1009-1013, Jul. 2000.

[23] W. Amrhein, S. Silber, K. Nenninger, "Levitation forces in bearingless permanent magnet motors," *IEEE Trans. on Magnetics*, vol.35, no. 5, pp.4052-4054, Sep. 1999.

[24] M. Amada, A. Mizuguchi, Y. Asano, J. Asama, A. Chiba, M. Takemoto, T. Fukao, "Winding Design and Characteristic of a Consequent-Pole Type Bearingless Motor with 4-Axis Active Magnetic Suspension," *Conference Record of the 2007 IEEE Industry Applications Conference 42nd IAS Annual Meeting*, pp.552-557, 23-27 Sept. 2007.

[25] D.P.M. Cahill, B. Adkins, "The permanent magnet synchronous motor," *Proc. Inst. El. Eng.*, vol. 109, no. 48, pp.483-491, Dec. 1962.

[26] A. Hamler, B. Hribernik, "Impact of shape of stator pole of one phase brushless motor on cogging torque," *IEEE Trans. on Magnetics*, vol.32, no.3, pp.1545-1548, May 1996.

[27] C. Breton, J. Bartolome, J.A. Benito, G. Tassinario, I. Flotats, C.W. Lu, B.J. Chalmers, "Influence of machine symmetry on reduction of cogging torque in permanent-magnet brushless motors," *IEEE Trans. on Magnetics*, vol.36, no.5, pp.3819-3823, Sep. 2000.

[28] Maxwell® 3D by Ansoft Corporation, http://www.ansoft.com.

[29] P. Karutz, T. Nussbaumer, W. Gruber, J.W.Kolar, "Saturation Effects in High Acceleration Bearingless Slice Motors, " *To be published in Proc. of the 2008 IEEE International Symposium on Industrial Electronics,* Cambridge (UK), 2008.

[30] R. Schoeb and J. Bichsel, "Vector control of the bearingless motor," *Proc. 4th Int. Symp. Magnetic Bearings*, Zurich, Switzerland, pp.327-332, 1994.

BIOGRAPHY

Philipp Karutz was born in 1981 in Magdeburg, Germany. He studied electrical engineering at Otto-von-Guericke University Magdeburg and received his M.Sc. degree in 2005. Since 2005 he was been with ABB Corporate Research Centre Baden, Switzerland working on EMC-simulations/measurements and the packaging of power modules for motor drives. He has been a Ph.D. student at the Power Electronic Systems Laboratory, ETH Zurich, Switzerland since 2006. His research interests include Power Factor Correction, ultra compact AC-DC converters and magnetically levitated motors. He is a student member of IEEE.

Thomas Nussbaumer was born in Vienna, Austria, in 1975 and studied electrical engineering at the University of Technology Vienna, Austria, where he received his M.Sc. degree with honors in 2001. During his Ph.D. studies at the Power Electronic Systems Laboratory (PES) in the Swiss Federal Institute of Technology (ETH) Zurich, Switzerland, he performed research on the design, control and modulation of three-phase rectifiers with low effects on the mains. After receiving his Ph.D. degree in 2004 he has been continuing research on power factor correction techniques, modeling and dynamic control of three-phase rectifiers and electromagnetic compatibility. Since Feb, 2006 he has been with Levitronix GmbH, where he is currently working on magnetically levitated rotors and pumps for the semiconductor process industry. Dr. Nussbaumer is a member of the Austrian Society of Electrical Engineering (OVE) and a member of the IEEE.

Wolfgang Gruber was born in Amstetten, Austria, in 1977. He studied mechatronics at Johannes Kepler University Linz, Austria, and received his M.Sc. degree in 2004. Since 2004, he has been a Scientific Assistant and Ph.D. student at the Institute of Electrical Drives and Power Electronics, Johannes Kepler University Linz, where he has been involved in various research projects. His research interests include magnetic bearings, bearingless motors and brushless motors. He is member of the Association for Electrical, Electronic & Information Technologies (VDE) and a student member of IEEE.

Johann W. Kolar (M'89–SM'04) received his Ph.D. degree (summa cum laude / promotio sub auspiciis praesidentis rei publicae) from the University of Technology Vienna, Austria. Since 1984 he has been working as an independent international consultant in close collaboration with the University of Technology Vienna, in the fields of power electronics, industrial electronics and high performance drives. He has proposed numerous novel PWM converter topologies, and modulation and control concepts, e.g., the VIENNA Rectifier and the Three-Phase AC-AC Sparse Matrix Converter. Dr. Kolar has published over 250 scientific papers in international journals and conference proceedings and has filed more than 70 patents. He was appointed Professor and Head of the Power Electronic Systems Laboratory at the Swiss Federal Institute of Technology (ETH) Zurich on Feb. 1, 2001.

The focus of his current research is on AC-AC and AC-DC converter topologies with low effects on the mains, e.g. for power supply of telecommunication systems, More-Electric-Aircraft and distributed power systems in connection with fuel cells. Further main areas are the realization of ultra-compact intelligent converter modules employing latest power semiconductor technology (SiC), novel concepts for cooling and EMI filtering, multi-domain/multi-scale modelling and simulation, pulsed power, bearingless motors, and Power MEMS. He received the Best Transactions Paper Award of the IEEE Industrial Electronics Society in 2005. He also received an Erskine Fellowship from the University of Canterbury, New Zealand, in 2003. In 2006, the European Power Supplies Manufacturers Association (EPSMA) awarded the Power Electronics Systems Laboratory of ETH Zurich as the leading academic research institution in Europe.

Dr. Kolar is a Member of the IEEE and a Member of the IEEJ and of Technical Program Committees of numerous international conferences in the field (e.g. Director of the Power Quality Branch of the International Conference on Power Conversion and Intelligent Motion). From 1997 through 2000 he has been serving as an Associate Editor of the IEEE Transactions on Industrial Electronics and since 2001 as an Associate Editor of the IEEE Transactions on Power Electronics. Since 2002 he also is an Associate Editor of the Journal of Power Electronics of the Korean Institute of Power Electronics and a member of the Editorial Advisory Board of the IEEJ Transactions on Electrical and Electronic Engineering.